AGU Advances

Key Points:

- Numerical simulations of mantle convection are coupled with the non-linear Liouville equation that governs polar motion dynamics
- True polar wander on the slow-rotating Venus is more similar to that on fast-rotating bodies such as Earth or Mars than previously thought
- We derive a scaling law for the mutual offset of spin and figure axes and argue that mantle flow does not generate the observed 0.5° offset

Correspondence to:

V. Patočka,
vojtech.patocka@matfyz.cuni.cz

Polar Motion Dynamics on Slow-Rotating Venus: Signatures of Mantle Flow

Vojtěch Patočka[1] , Julia Maia[2] , and Ana-Catalina Plesa[2]

[1]Department of Geophysics, Charles University, Prague, Czech Republic, [2]Institute of Space Research, German Aerospace Center (DLR), Berlin, Germany

Abstract With its 1 day lasting 243 days on Earth, Venus is the slowest-spinning planet in the Solar System and its rotational bulge is anomalously small. A rotational bulge stabilizes the orientation of planets. Having only a tiny stabilizer, the rotational pole of Venus has been expected to separate from the figure pole in response to mantle flow, which has been used to explain why both poles are observed to be 0.5° apart. Here, we couple 3D mantle-convection simulations and polar motion dynamics to explore how mantle flow, and in particular surface mobilization, drives Venus's polar motion. We provide a predictive framework for polar motion on slow rotators and show that the spin/figure pole separation (or offset) follows a simple law: it scales with the figure-axis drift rate times the planet's Chandler period. Contrary to prior expectations, stronger internal loading does not amplify the offset, and the mantle-driven polar motion is smooth rather than wobbly, more similar to that of fast rotators. In models matching Venus's geoid, figure-axis drift rates reach only up to a few °/Myr, too slow compared to ca. 60°/Myr that is needed to match the observed offset. We therefore exclude mantle convection as the cause of Venus' spin and figure poles separation, and suggest that atmospheric and solid tides are not balanced instead.

Plain Language Summary In response to various geological processes such as mantle convection or volcano formation, the rotational pole of a planet may move on its surface. This phenomenon is called true polar wander (TPW) and it is known to operate differently on Venus when compared to planets such as Earth and Mars, because Venus rotates very slowly. On Venus, the spin axis has been expected to separate from the figure axis during TPW, which is consistent with the observed, relatively large separation of both of these axes on Venus (0.5°, figure axis reflects the density structure of the planet). Here we show that when mantle convection is simulated with a state-of-the-art numerical model that accounts for the slow and continuous nature of mantle flow, TPW on the slow-rotating Venus is more similar to TPW on all other planets. We derive an equation that can be used to predict how much the spin and figure axes separate during TPW and argue that mantle convection is not responsible for the observed 0.5° offset. Therefore, other mechanisms must be involved, implying that the moments of forces exerted on Venus by the atmosphere and by the Sun are not balanced.

1. Introduction

On most planets, the deviation from spherical shape is driven primarily by rotation. The polar and equatorial radii of Earth differ by 21 km and this circumequatorial excess mass acts as a stabilizing anchor, firmly binding the rotation vector ω to the figure axis (or main axis of inertia, MIA). In equilibrium, planetary bodies spin around the figure axis: ω and MIA are exactly aligned. When perturbed, the rotation pole exhibits a circular motion (wobble), a phenomenon first observed by the astronomer S.C. Chandler. With respect to stars, ω stays approximately fixed, and it is the figure of the planet that periodically changes its orientation. To estimate the present-day wobble amplitude, one typically measures the angular distance between both axes (Gross, 2000; Spada et al., 1996) (here labeled α). On Earth, the Chandler wobble has a radius of less than 5 m ($\alpha < 0.2''$), as its main drivers, atmospheric and ocean dynamics (Gross, 2000), are weak compared to the stabilizing mass of the rotational bulge. On geological time scales, the figure and rotation poles are assumed to coincide (Ricard et al., 1993). In other words, on Earth, the Chandler wobble and the secular motion of the solid surface relative to the rotation pole (true polar wander) have different origins and are treated separately when the polar path is analyzed.

Venus, on the other hand, rotates slowly. The planet has a retrograde, 243-day long rotation period, which generates an equatorial bulge of a few tens of centimeters in amplitude if rotation only is considered. Such a small bulge translates into a small difference between the main moment of inertia C and the minor moment of inertia A,

Writing – original draft: Vojtěch Patočka
Writing – review & editing: Julia Maia,
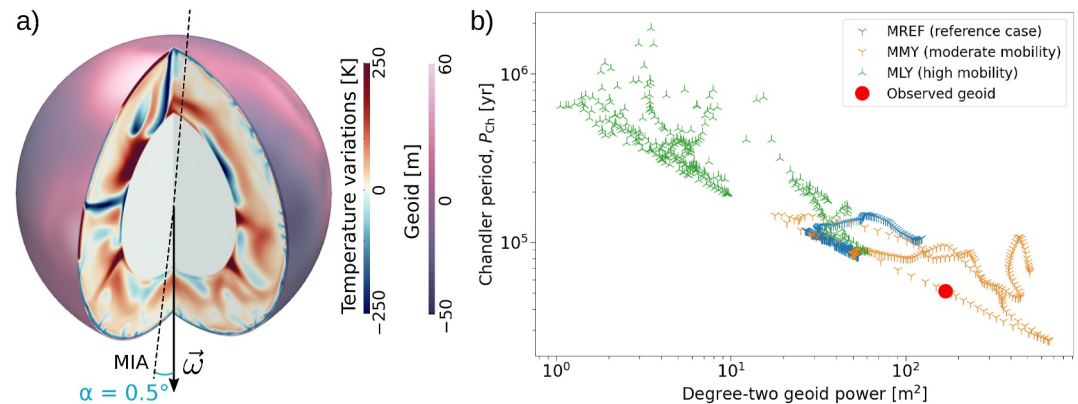Ana-Catalina Plesa

Figure 1. (a) Snapshot of the temperature anomalies in model MMY and the resulting geoid height. The angular difference between the main axis of inertia MIA and the rotation vector $\boldsymbol{\omega}$ is denoted by α. The observed value is $\alpha = 0.5°$ (Konopliv et al., 1999). (b) Relationship between the geoid power at the spherical harmonic degree 2 and the Chandler period P_{Ch} (Equation 2). Points show evenly sampled snapshots in time from each numerical simulation (different symbols represent different models), red circle shows the observed geoid of Venus (Konopliv et al., 1999). Simulation data mostly lie in a narrow band, implying that moments of inertia differences $C-A$ and $C-B$ typically do not go to zero, that is, that the mantle flow breaks the symmetry of the body in a way that is consistent with the observed geoid components (cf. Equation 2).

of only 3.4×10^{30} kg m^2 (Appendix A), which corresponds to dynamic flattening $(C-A)/C = 5.7 \times 10^{-8}$. However, from the observed gravity field of Venus (Konopliv et al., 1999), the dynamic flattening is 1.7×10^{-5}, more than two orders of magnitude larger than the value derived from rotation only (but still much smaller than Earth's 3.3×10^{-3}). Hence, unlike all other planets in the Solar System, the long-wavelength shape of Venus is not dominated by its rotation. Its principal moments of inertia must result from other sources, such as dynamic topography generated by convective flow in the mantle, a fossil shape, or large uncompensated topography.

A related striking property associated with Venus' rotation dynamics is the large angular difference between the rotation axis and the figure axis (Figure 1). The observed value $\alpha = 0.5°$ (Konopliv et al., 1999) relies on an accurate determination of the spin state (Davies et al., 1992; Margot et al., 2021), and suggests that Venus should have a uniquely large amplitude wobble. This motivated Spada et al. (1996) to investigate whether mantle convection could drive the planet's wobbling (cf. also Yoder & Ward, 1979). Spada et al. (1996) showed that the rotational and figure poles of slow rotators separate during true polar wander and seemingly explained the angular offset α. When averaged over time, the obtained value was comparable to $0.5°$. The study simulated mantle flow as a series of randomly distributed internal point loads mimicking subducting slabs. As a result, the pole path consisted of large spiral segments triggered by individual loads and α showed a large temporal variance, sometimes exceeding $10°$. However, the stepwise perturbations from point loads do not adequately portray the slow and continuous mantle flow and are inconsistent with the observed geoid.

Here, the possibility of an internally driven wobble is revisited using global 3D thermal evolution models of mantle convection for different geodynamic regimes, since the latter remains enigmatic on Venus. Observational data do not support the existence of continuous plate tectonics as on Earth, but recent evidence of ongoing geological activity (Herrick & Hensley, 2023; S. E. Smrekar et al., 2010; Sulcanese et al., 2024) and crater statistics analyses (O'Rourke et al., 2014) indicate that the planet is unlikely to be in a stagnant lid regime (Rolf et al., 2022), as is the case for Mars and Mercury.

We investigate how mantle convection, with fine temporal resolution and realistic geoid signature, is imprinted into the polar motion dynamics of slow-rotating planets. In particular, models with different surface mobility are compared in terms of the resulting α, and also the relative paths of the rotation and figure poles are analyzed, a feature that can be of interest in the context of the upcoming missions to Venus, VERITAS (S. Smrekar et al., 2022) and EnVision (Grete Straume-Lindner et al., 2022). We show that true polar wander on fast and slow rotators behaves more similarly than previously thought, and derive a scaling law for the angular offset α.

2. Polar Motion Driven by Mantle Convection

We perform global mantle convection simulations in a 3D spherical geometry adopting the code GAIA-v2 (Hüttig et al., 2013) to model Venus' thermal evolution over 4.5 Gyr and employing parameters representative for the interior of Venus, assuming a liquid core (Table B1). We consider partial melt production (Padovan et al., 2017) and extract the produced melt both extrusively at the surface and intrusively within the lithosphere. Given the uncertainties regarding Venus' tectonic regime and crustal recycling (Rolf et al., 2022), we focus on investigating models with different levels of surface mobility. The details of the code and model setups are provided in Methods (Appendix B).

Our reference scenario (MREF) represents the so-called plutonic squishy lid regime (Lourenço et al., 2020) where most of the produced melt is placed within the lithosphere. The model has a reference viscosity of 10^{21} Pa s and assumes that 80% of the melt is placed intrusively at a depth of 45 km while the remaining melt is placed extrusively at the surface. No plastic yielding is included, but small-scale surface mobilization can happen due to weakening of the lithosphere after the emplacement of large volumes of magmatic intrusions.

Higher levels of surface mobilization and lithospheric recycling can be obtained by considering a pseudo-plastic rheology. The yield stress value controls the level and behavior of surface mobilization. Adopting a moderate yield stress value (30 MPa, model MMY) results in sporadic surface mobilization events and can be interpreted as in-between plutonic-squishy lid and episodic lid regimes. When the yield stress is further reduced (19 MPa, model MLY), the simulation shows continuous surface mobilization (so-called mobile-lid regime).

In each simulation, we extract the evolving inertia tensor $I_{MC}(t)$ from the degree-2 geoid anomalies generated by mantle convection. The tensor is combined with the rotational bulge contribution, $I_{RB}(t)$, together forming the total inertia tensor $I(t)$ that enters the Liouville equation (Appendix A), which is solved to determine the rotation vector evolution in the body-fixed frame (polar motion). While the simulated time is 4.5 Gyr, we select only the last 0.5 Gyr to compute the polar motion.

Owing to Venus' small rotational bulge, the perturbations of the total inertia tensor are dominated by mantle convection. Hence, the main axis of I_{MC} (named MIA-MC) and of I (MIA) nearly coincide and we refer to both simply as MIA or figure pole (with the exception of the fossil shape analysis in Section S3 in Supporting Information S1). This stands in contrast to fast rotators, where the large rotational bulge acts as a low-pass filter of the convective signals and delays MIA with respect to MIA-MC by up to a few degrees (Cambiotti et al., 2011).

Figure 2 illustrates the dynamics of polar motion in response to mantle flow for a slow-rotating planet. The time evolution of the figure pole in the MMY model is shown as a path on the unit sphere (Figure 2c). The movement of MIA is driven by the slow reorganization of mantle plumes and by episodes of increased surface mobility. Its speed stays below 1.5°/Myr. During the 0.5 Gyr window, MIA moves by tens of degrees in total, whereas α is only a small fraction of a degree—the paths of the figure and rotation poles are thus indistinguishable on the geological timescale, similarly to the theory of fast rotators (e.g., Earth, Mars). The angular offset α is at all times smaller than 0.05°, an order of magnitude below the observed value, the time-average being another order of magnitude lower (gray dashed line in Figure 2e).

To understand how the figure pole drift drives polar motion, we performed a series of synthetic tests in which the inertia tensor is artificially controlled by imposing a time-evolving surface load, in which the MIA direction and speed are arbitrarily varied (Figures 2a and 2b and Section S1 in Supporting Information S1). As soon as the figure pole sets out, the rotation pole also starts to move, but in a perpendicular direction, consistent with the linear analysis of the Liouville equation in the limit of slow-rotators (Spada et al., 1996).

The faster the figure pole moves, the more the rotational pole departs from it, because both poles are moving in different directions. Hence, the angular speed of the figure pole (MIA rate) drives the increase of α. However, this increase is not unlimited. The natural timescale over which the rotation pole velocity changes direction and α stops growing is the Chandler period. Therefore, the angular separation of the figure axis and the rotation axis, α, should be proportional to the MIA rate times P_{Ch}.

During the initial, straight segment of the figure pole, the rotation pole draws half-ellipses along the right side of the MIA path ("scalloped" behavior, Figures 2a and 2b; one scallop lasts P_{Ch}). During this stage, α oscillates from 0 to (MIA rate)P_{Ch}/π, averaging at half of the maximum value. Rapid changes in the direction or speed of the
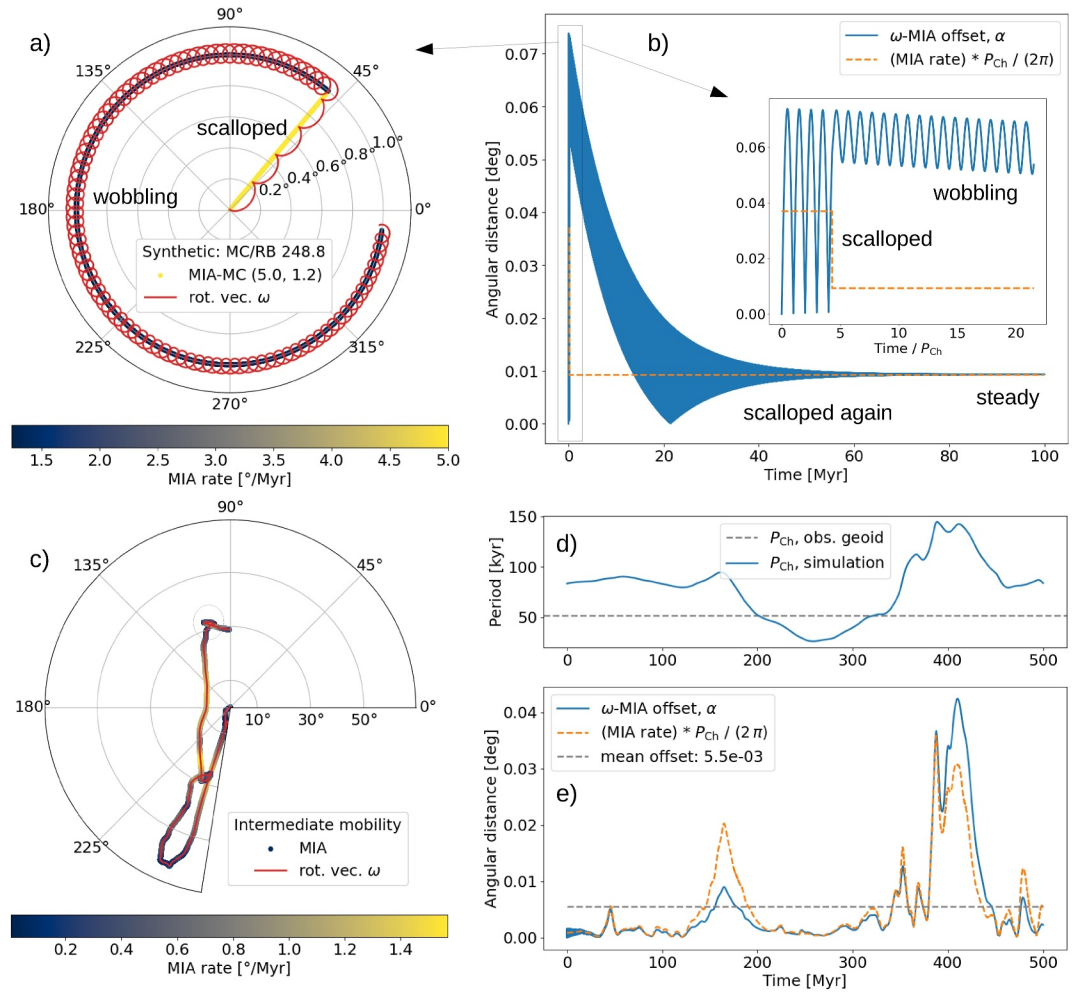
Figure 2. Polar motion response of Venus. (a, b) Synthetic tests in which the internal loading, $I_{MC}(t)$, is artificially prescribed, with MIA-MC moving first straight at the rate of 5°/Myr (polar motion is scalloped) and then abruptly slowing down to 1.2°/Myr (the change induces wobbling). The imposed difference between the main and the minor moments of inertia ($C-A$) is two orders of magnitude larger than $C-A$ of the rotational bulge (MC/RB), similarly to values obtained from the observed geoid. In steady state, the angular offset between the spin and figure axes α follows Equation 1, shown by the orange dashed line. (c–d) Mantle convection simulation with moderate surface mobility (MMY). Paths of the rotational and figure poles on the globe (c), the evolution of Chandler period, P_{Ch}, as computed via Equation 2 from the mantle flow-induced geoid (d), and the time evolution of α, compared with our scaling law, Equation 1 (panel e, blue vs. orange lines). The average angular separation of the figure and rotation axes is two orders of magnitude below the observed value (gray dashed line).

figure pole trigger wobbling, during which α reflects the pre-change MIA rate (Figure 2b). However, if the figure pole moves steadily, the average value of α always returns to 0.5 (MIA rate) P_{Ch}/π due to viscous dissipation. In steady state, the rotational pole moves smoothly, following the figure pole on its right-hand side (Figure S1h in Supporting Information S1).

In our mantle convection simulations (MREF, MMY, and MLY), the figure pole path is a natural response to mantle flow. At the onset of polar motion, scalloped behavior lasts about 30 Myr (blue line in Figure 2e appears thick), but once the oscillations decay they do not reappear—the natural jerks in the figure pole trajectory are not rapid enough to excite wobbling. After the initial transient stage, ω and MIA move parallel to each other and α is reasonably well captured by the law obtained in synthetic tests:

$$\alpha \approx \frac{d(\text{MIA})}{dt} \frac{P_{Ch}}{2\pi}, \tag{1}$$

where d(MIA)/dt is the angular speed of the figure pole. Discrepancies generally depend on the direction of the figure pole acceleration, with sudden moves toward the rotation axis decreasing the mutual offset and vice versa.

The Chandler period P_{Ch} is related to the Euler period—the free wobble period of rigid bodies—through a factor that accounts for the elastic readjustment of the rotational bulge (Munk & MacDonald, 1975; Patočka & Walterová, 2025). Such an approach is necessary only when the shape of the body is dominated by rotation, which is not the case for Venus, whose secular Love number is anomalous (Burša, 1984; Patočka & Walterová, 2025). Hence, we can approximate the Chandler period simply as the Euler period,

$$P_{Ch} \approx P_E = \frac{2\pi}{\omega_0}\sqrt{\frac{AB}{(C-A)(C-B)}}. \tag{2}$$

With MIA-MC $\approx$ MIA and $P_{Ch} \approx P_E$, the reorientation dynamics of Venus are seemingly similar to those of a rigid body, while for other bodies in the Solar System the rotational bulge and its readjustment are important features (Matsuyama et al., 2014; Patočka & Kihoulou, 2023). In the context of Venus, the rotational bulge relaxation enters merely in that it defines the time scale at which viscous dissipation dampens the oscillations of α and the polar motion becomes steady.

The relationship derived here, Equation 1, marks a key paradigm shift in our understanding of polar motion on slow rotators. Large amplitudes of the load compared to the rotational bulge do not enable large-scale wobbling (and high α values). Instead, we show that α is controlled by the drift velocity of the figure axis (MIA rate), which is governed solely by the slow mantle circulation, and by the Chandler period. The Chandler period is inversely affected by the internal load strength. This relationship is illustrated in Figure 1b, where the load strength is represented in terms of the degree-2 geoid power. Thus, strong loading tends to suppress, rather than promote, large offsets between the spin and figure axes (see Figure S2a in Supporting Information S1 for a comparison with the original work of Spada et al. (1996)).

With the rotation axis staying close to the main inertia direction of mantle convection (MIA-MC) on geological time scales, the obtained true polar wander is similar to that on other planets (Ricard et al., 1993). This contrasts with the mega-wobble scenario in which the rotation pole moves along large-angle circular segments, as presented in Spada et al. (1996) or Hu et al. (2017). The difference lies in the significantly larger and continuous load amplitude investigated here.

While the load size is prescribed as a certain fraction ($\sim 10^{-5}$) of Venus' mass by Spada et al. (1996), in our simulations it is controlled by the height of the mantle flow-derived geoid. In model MMY, the geoid power is comparable to the observed one, but in models MREF and MLY it is lower (Figure 1). It cannot be excluded that part of Venus's geoid originates from uncompensated surface features or from a fossil shape (Zharkov et al., 2019). In Section S3 in Supporting Information S1, we investigate the possibility that Venus is only partially shaped by convection at present. In this additional simulation, the rotation pole still follows the figure pole and Equation 1 is satisfied. The obtained offset is, however, even smaller, because the overall MIA rate is reduced by the presence of the static contribution to the inertia tensor (i.e., by the fossil contribution).

Since the rotational bulge plays only a small role in the obtained polar motion, key parameters of this study are those governing the mantle flow. Increasing or decreasing the reference viscosity, $\eta = 10^{21}$ Pa s, by up to one order of magnitude does not have a significant effect on the presented results. Some of our preliminary tests indicate that lower viscosity leads to smaller geoid and higher MIA rates, but making general conclusions about the relationship between mantle viscosity, the geoid, and the MIA rate requires a thorough statistical analysis, outside the scope of the present work whose focus is on the polar motion dynamics.

3. Figure Pole Drift Rates and the Relative Paths

In Figure 1b, the simulated degree-2 geoid amplitude is plotted against the Chandler period. There is a clear negative correlation: the larger the geoid signal, the smaller the P_{Ch}. The filled red circle marks the observed geoid of Venus (Konopliv et al., 1999), which lies within the band obtained from our numerical simulations, in line with the hypothesis that the long-wavelength density structure and shape of Venus are dominated by mantle convection (James et al., 2013; Maia et al., 2023; Pauer et al., 2006).
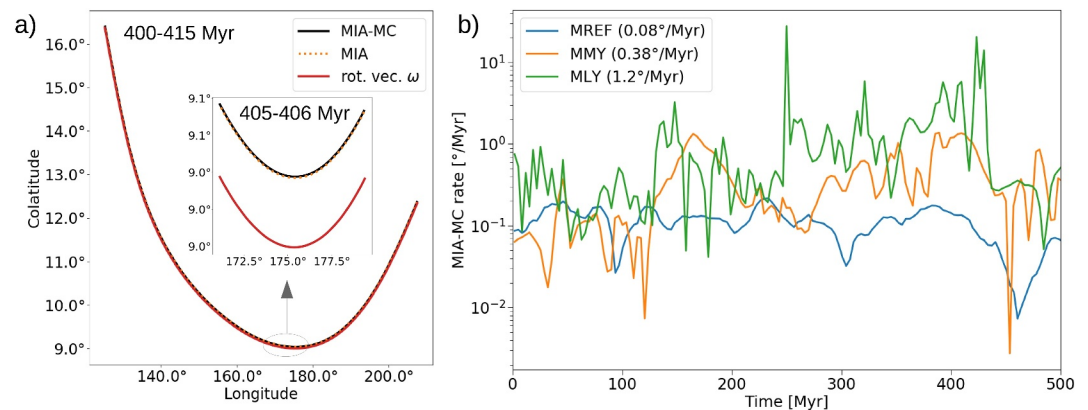
Figure 3. (a) Zoom-in to a 15 and 1 Myr (inset) time windows, showing the smooth path of the rotation pole even during one of the "jerks" in which the figure pole velocity rapidly changes direction (the selected window is indicated by the black circle near the end of the polar path in Figure 2c). (b) Time evolution of the figure-axis drift rate in models with different surface mobilities. The mean value is stated in the legend and stays firmly below the critical value of 60°/Myr in all three simulations.

Assuming a 1D density profile consistent with the mass of Venus (Methods), the gravity data can be converted to the moments of inertia A, B, C using MacCullagh relations, and Equation 2 then gives $P_{Ch} \approx 50$ kyr (marked as "observed geoid" in Figure 1b). Using this value, Equation 1 requires the figure pole to drift at approximately 60°/Myr to separate ω from MIA by 0.5°. In this section we argue that such high values of the MIA rate are unlikely regardless of the tectonic regime.

The average figure pole speed increases with increasing surface mobility (Figure 3b), but even for the mobile-lid case MLY it is only ~ 1°/Myr, much less than the critical rate of 60°/Myr. For a comparison, despite the operation of plate tectonics, the typical MIA rate on Earth is expected to be <0.2°/Myr (Richards et al., 1997) (although some rapid episodes of true polar wander have been proposed on the basis of reconstructed plate motion velocities (Steinberger & Torsvik, 2008)).

Despite the chaotic and fast MIA trajectory, the jerks in the figure pole velocity are not sufficient to disrupt the steady-state polar motion in models MREF and MMY (Figure 3a). Our results thus indicate that the internally driven polar motion should be parallel to that of the figure pole, its speed staying below ~ 1°/Myr, which corresponds to ~ 0.1 m/yr on the surface of Venus.

Direct detection of the secular motion of Venus's surface is limited by radar tie points sensitivity, which is 5–10 m laterally over the whole time span of VERITAS (Cascioli et al., 2023). A more promising method for estimating the direction and speed of polar motion is to compare the rotation pole position with the one recorded decades ago (using Magellan images and those from VERITAS or EnVision (Cascioli et al., 2021)). Evaluating the figure pole motion additionally requires an analysis of the time evolution of the degree-2 gravity coefficients in the body-fixed frame. In our simulations, the time derivatives of C_{21}, S_{21}, and S_{22} reach only $\sim 10^{-14}$/yr, while the uncertainty in measuring these degree-2 coefficients by VERITAS is on the order of 10^{-11} (Giuliani et al., 2025). Therefore, our predicted true polar wander signature is likely below the observational threshold of the upcoming missions.

To disrupt a steady polar motion, that is, to trigger a scalloped or wobbling behavior, the figure pole velocity must undergo significant changes in amplitude or direction on a time scale comparable to the Chandler period. In the model with high surface mobility, MLY, a few transitions between the different qualitative behaviors are experienced. For instance, after two very brief episodes of flow reorganization during which the MIA rate exceeds 10°/Myr (Figure 3b). Note, however, that while the geoid amplitude is in agreement with the observed geoid in model MMY (Figure 2d), it is not the case in the high mobility case MLY. The non-trivial behavior in model MLY is related to its unrealistically low geoid amplitude, hence large P_{Ch} (Figure 1b). It is a result of the Chandler period occasionally exceeding 1 Myr, making the figure pole jerks relatively more rapid. Such a scenario can be excluded for present day Venus, as it is inconsistent with the observed geoid.

4. Discussion

We have analyzed the polar motion response of slow-rotating planets to internal loading, testing the hypothesis that the angular offset between the rotation and figure poles of Venus is driven by mantle convection. We derived a scaling law, Equation 1, which implies that the figure pole has to move at $\approx 60°/$Myr to explain the observed $\alpha = 0.5°$ offset. Using 3D spherical mantle convection simulations with variable surface mobility, we showed that the obtained rates were one to three orders of magnitude smaller.

We model Venus as a free rotator, neglecting external torques. This means that the solar gravitational torques, acting on the thermal and solid body tides, are assumed balanced, which results in a stable rotation relative to stars (non-stationarity in the body-fixed frame is a direct consequence of the non-zero α value). Mutual balance between atmospheric and solid tides is commonly assumed in order to explain the slow retrograde rotation of Venus in the first place (Correia & Laskar, 2001, 2003; Dobrovolskis & Ingersoll, 1980; Musseau et al., 2024; Revol et al., 2023; Yoder, 1995), but recent measurements of the spin axis precession imply a non-zero net torque (Margot et al., 2021). The way in which atmospheric circulation drags the surface of Venus is unclear. Apart from surface friction from the wind and gravitational coupling between mass of the atmosphere and that of the solid, there may be a significant role of mountain waves (Navarro & Schubert, 2024; Navarro et al., 2018). If internal forces are unlikely to separate the rotation and figure axes, as our results suggest, then external forces are the probable cause, indicating that the torques acting on the solid Venus are not balanced and its rotation state is still evolving.

Future studies should examine how tidal forcing affects the derived rotational law (Equation 1). We note that considering tidal forcing may shorten the Chandler period (Phan & Rambaux, 2025), which would further reduce the predicted value of the internally generated value of α.

While the polar motion dynamics of slow and fast rotators are, in some aspects, fundamentally different, we argue that true polar wander of Venus may be more similar to that of Earth and Mars than previously thought—on geological timescales, the rotation pole follows the main inertia direction of mantle convection. Recent analysis of misaligned parabola-shaped dust deposits on Venus's surface indicates that Venus has reoriented by 10–20° in the past tens of Myr (Austin et al., 2025), implying a moderate true polar wander rate.

On Earth, it is speculated that the orientation of the mantle is controlled by a deep degree-2 structure, the large low-shear-velocity provinces and plumes rising from their edges (Dziewonski et al., 2010; Torsvik et al., 2010). Although our geodynamic models do not indicate any prominent degree-2 structure, it is tempting to speculate that plume clusters anchor also the mantle of Venus. The Beta-Atla-Themis (BAT) province is dominated by a high concentration of volcanic rises, interconnected by rift systems and tectono-magmatic structures (Johnson & Richards, 2003), probably with ongoing or recent volcanoes (Herrick & Hensley, 2023) indicating mantle plumes as the source of the geological activity. Similarly to fast rotators that have prominent features near the equator, the BAT province is located in the equatorial region of Venus.

Appendix A: LIOUSHELL—Liouville Equation Solver for Viscoelastic Planetary Shells

In order to couple the interior and rotational dynamics and hence simulate the polar motion of Venus, two sets of equations need to be solved. The first set describes the viscoelastic response to changes in the direction or speed of the rotation vector. The second set are the Liouville equations, which determine the time evolution of the rotation vector $\boldsymbol{\omega}(t)$. The numerical method used here was benchmarked and described in more detail in Patočka et al. (2018) and Patočka (2021). The method is briefly repeated below.

The viscoelastic response of a hydrostatically prestressed, radially stratified spherical shell (i.e., the time evolution of the rotational bulge, $\boldsymbol{I}_{RB}$) is obtained by integrating the following set of partial differential equations:

$$\nabla \cdot \boldsymbol{\tau} - \left(\boldsymbol{u} \cdot \nabla \rho_0 \right) \boldsymbol{g}_0 - \rho_0 \nabla (\Phi + \Theta) = 0, \tag{A1}$$

$$\nabla \cdot \boldsymbol{u} = 0, \tag{A2}$$

$$\boldsymbol{\tau}^d - \mu\big(\nabla\boldsymbol{u} + (\nabla\boldsymbol{u})^{\mathrm{T}}\big) = -\frac{\mu}{\eta}\int_0^t \boldsymbol{\tau}^d \mathrm{d}t', \tag{A3}$$

representing respectively the conservation of momentum, incompressibility, and the Maxwellian viscoelastic rheology. The Cauchy stress tensor is denoted by $\boldsymbol{\tau}$, $\boldsymbol{\tau}^d$ is its deviatoric part, ρ_0 is the 1D density profile of the undeformed (reference) configuration of the body, $\boldsymbol{u}$ is the displacement field, μ is the elastic shear modulus, η is the viscosity, t is the time, and Φ and Θ are defined below (Equation A5).

In the deformed state, the Eulerian density increment of the incompressible body is given as,

$$\delta\rho\,(\boldsymbol{r},t) = \rho(\boldsymbol{r},t) - \rho_0(r) \cong -\boldsymbol{u}(\boldsymbol{r},t)\cdot\nabla\rho_0(r), \tag{A4}$$

Therefore, the second term on the LHS of Equation A1 is the body force $\delta\rho\,\boldsymbol{g}_0$. The potentials Φ and Θ are respectively the self-gravity and the centrifugal potentials,

$$\Phi(\boldsymbol{r},t) = -G\int_{v(t)}\frac{\delta\rho(\boldsymbol{r}',t)}{|\boldsymbol{r}-\boldsymbol{r}'|}\,\mathrm{d}v', \quad \Theta(\boldsymbol{\omega},\boldsymbol{r}) = \frac{1}{2}\big((\boldsymbol{\omega}\cdot\boldsymbol{r})^2 - |\boldsymbol{\omega}|^2|\boldsymbol{r}|^2\big) \tag{A5}$$

The outer boundary condition mimics a free surface. A liquid core in hydrostatic equilibrium is assumed to reorient along with the mantle (assuming a rotationally decoupled core shortens the Chandler period by a few tens of percent but does not change the results qualitatively).

To compute the temporal evolution of the angular velocity vector $\boldsymbol{\omega}$ with respect to the body-fixed Tisserand frame (Munk & MacDonald, 1975), the Liouville equations with zero external torque are solved,

$$\frac{\mathrm{d}\boldsymbol{\omega}}{\mathrm{d}t} = -\boldsymbol{I}^{-1}\cdot\left(\frac{\mathrm{d}\boldsymbol{I}}{\mathrm{d}t}\cdot\boldsymbol{\omega} + \boldsymbol{\omega}\times(\boldsymbol{I}\cdot\boldsymbol{\omega})\right), \tag{A6}$$

where $\boldsymbol{I}$ is the time dependent tensor of inertia, representing both the rotational bulge and the signal from mantle convection, $\boldsymbol{I}(t) = \boldsymbol{I}_{\mathrm{RB}}(t) + \boldsymbol{I}_{\mathrm{MC}}(t)$. Equation A6 is the conservation of the angular momentum, $\boldsymbol{I}\cdot\boldsymbol{\omega}$, expressed in the rotating geographic frame. Equations A1–A3 are mutually coupled with Equation A6 through the displacement field $\boldsymbol{u}$, which is needed to compute the inertia tensor $\boldsymbol{I}_{\mathrm{RB}}$ (MacCullagh's formulae, given in terms of the self-gravity potential Φ in Equation 14 of Patočka et al. (2018)), and through the centrifugal potential Θ, which depends on the angular velocity vector $\boldsymbol{\omega}(t)$. $\boldsymbol{I}_{\mathrm{MC}}(t)$ is computed from mantle convection simulations as described in Appendix B.

Prior to each simulation, we let the body spin for 10 Gyr to reach rotational equilibrium. Therefore, at the time $t = 0$, the body has a fully developed rotational bulge. In order to avoid unrealistic stepwise jump of the figure pole at the beginning of each simulation, we rotate $\boldsymbol{I}_{\mathrm{MC}}$ to make it initially aligned with the z-axis. In this way, the figure pole path is continuous and only the MIA-MC rate, that is, only the first derivative, experiences a jump at the beginning of each simulation. Radial profiles of the model are described in Appendix B, the elastic shear modulus is assumed depth-constant, $\mu = 100$ GPa.

Appendix B: 3D Mantle Convection Simulations Using GAIA

We use the finite volume, mantle convection code GAIA-v2 (Hüttig et al., 2013) in a full 3D spherical shell geometry to model the thermal evolution of Venus' interior. We solve the conservation equation of mass, linear momentum, and thermal energy on a fixed grid with 3.6 million computational cells (i.e., 40,962 lateral and 87 radial points), resulting in 30 km radial resolution in the mantle and 106 km at the planetary surface. The non-dimensional equations read:

Table B1
Parameters Used in the Geodynamical Simulations

Symbol	Description	Value
D	Mantle thickness	2,550 km
T_{ref}	Reference temperature	1600 K
z_{ref}	Reference depth	102.5 km
E	Activation energy	154.3×10^3 J mol^{-1}
V_{ref}	Activation volume at the surface	4.3×10^{-6} m^3 mol^{-1}
T_{surf}	Surface temperature	737 K
T_{init}	Initial temperature at the top of the convecting mantle	1800 K
ΔT	Initial temperature drop across the mantle	3263 K
T_{CMB}	Initial core-mantle boundary temperature	4000 K
α_V	Reference thermal expansivity	3×10^{-5} K^{-1}
η	Reference viscosity	10^{21} Pa s
μ	Shear modulus	10^{11} Pa
c_p	Reference heat capacity	1,142 J kg^{-1} K^{-1}
ρ	Reference density	3,300 kg m^{-3}
c_c	Core heat capacity	850 J kg^{-1} K^{-1}
ρ_c	Core density	7,000 kg m^{-3}
g	Surface gravity acceleration	8.87 m s^{-2}
k	Reference thermal conductivity	2.3 W m^{-1} K^{-1}
κ	Mantle thermal diffusivity	6.1×10^{-7} m^2 s^{-1}
Q	Total initial radiogenic heating	23.5×10^{-12} W kg^{-1}
σ_y	Yield stress	1.88×10^7, 3×10^7 Pa

Note. The values for the activation energy and activation volume are scaled in order to mimic a non-Newtonian rheology (see text for further details).

$$\nabla \cdot \tilde{v} = 0,$$
$$\nabla \cdot \left[\eta \left(\nabla \tilde{v} + (\nabla \tilde{v})^T \right) \right] - \nabla p + Ra\ \alpha T\ \tilde{e}_r = 0,$$
$$\frac{\partial T}{\partial t} + \tilde{v} \cdot \nabla T - \nabla \cdot (k \nabla T) - Di\ \alpha (T + T_0) v_r - \frac{Di}{Ra} \Psi - H = 0, \tag{B1}$$

where $\tilde{v}$ is the velocity vector, v_r is its radial component, η is the viscosity, p is the dynamic pressure, α is the thermal expansivity, T is the temperature, $\tilde{e}_r$ is the unit vector in radial direction, t is the time, k is the thermal conductivity, Di is the dissipation number, T_0 is the non-dimensional surface temperature, and Ψ is the viscous dissipation, that is, the product of the deviatoric stress and strain-rate tensors. The list of parameters used in this study is given in Table B1.

The thermal Rayleigh number (Ra), the internal heating rate (H), and the dissipation number Di are calculated as follows:

$$Ra = \frac{\rho g \alpha \Delta T D^3}{\eta \kappa}, \quad H = \frac{\rho\ Q_{HPE} D^2}{k \Delta T}, \quad Di = \frac{\alpha g D}{c_p}, \tag{B2}$$

where g is the gravitational acceleration, Q_{HPE} is the internal heat production rate in W kg^{-1}, and c_p is the mantle heat capacity.

Our models use a pressure and temperature dependent viscosity following the Arrhenius law. Its non-dimensional form reads (Roberts & Zhong, 2006):

$$\eta(T,z) = \exp\left(\frac{E + zV(z)}{T + T_0} - \frac{E + z_{\text{ref}}V(z)}{T_{\text{ref}} + T_0}\right), \tag{B3}$$

where z is the depth, z_{ref} and T_{ref} are the reference depth and temperature where the reference viscosity is attained, and E and V(z) are the activation energy and the depth-dependent activation volume, respectively. The activation energy E controls the temperature dependence of the viscosity, and the activation volume V determines the viscosity increase with depth (Hirth & Kohlstedt, 2003). For all our models we assume a dry, non-Newtonian rheology and mimic the behavior of dislocation creep by employing a Newtonian viscosity and dividing the activation energy and activation volume by the stress exponent (Christensen, 1984). In the reference case (MREF), we employ a depth-dependent activation volume (Tackley et al., 2013), setting $dV/dz = -2.3 \times 10^{-13}$, decreasing the activation volume from $V_{\text{ref}} = 4.3 \times 10^{-6}$ m^{-3}mol^{-1} at the surface to $V_{\text{cmb}} = 3.5 \times 10^{-6}$ m^{-3}mol^{-1} at the CMB. The resulting viscosity increase with depth is about two orders of magnitude, consistent with constraints from gravity–topography correlation analyses (Pauer et al., 2006; Rolf et al., 2018). For cases with surface mobility, we adopted depth-constant activation volume, $dV/dz = 0$, resulting in a three-order-of-magnitude increase to produce larger, more buoyant plumes capable of stronger surface mobilization.

In the models MLY and MMY, we use pseudo-plastic yielding and allow the stagnant lid to self-consistently fail when convective stresses exceed a prescribed yield stress σ_y. In this case the effective viscosity reads:

$$\eta_{\text{eff}} = \left[\eta(T,z)^{-1} + \left(\frac{\sigma_y}{2\dot{\varepsilon}}\right)^{-1}\right]^{-1}, \tag{B4}$$

where σ_y is the yield stress, and $\dot{\varepsilon}$ is the second invariant of the strain rate tensor. We use a yield stress values of 3×10^7 Pa for MMY and 1.88×10^7 Pa for MLY in order to obtain a higher surface mobility. While yield stress values adopted here are much lower than experimentally determined values (~700 MPa, Kohlstedt et al., 1995), this discrepancy between geodynamical models with plate tectonics-like behavior and laboratory studies is well-known and stems from the simplifications that global geodynamical models need to adopt when modeling brittle deformation (Van Zelst et al., 2022).

The thermal expansivity and thermal conductivity used in our models are also pressure and temperature dependent and follow the parametrization in Tosi et al. (2013). Moreover, we account for radioactive decay and core cooling. For the radioactive decay of heat producing elements we use the heat production rate and half-lives of radioactive isotopes (i.e., ^{235}U, ^{238}U, ^{232}Th, ^{40}K) together with Equation 1 and parameters from Breuer (2009) to update the total heat production rate at each step of the simulation. For the evolution of the core, we use a 1D energy balance at the bottom boundary to update the temperature at the core-mantle boundary at each time step (Stevenson et al., 1983).

Our models consider melting in the mantle using the method by Padovan et al. (2017) and comparing at each time step the mantle temperature with the local solidus (Stixrude et al., 2009). Melt is extracted from the mantle assuming that 20% will reach the surface while 80% remains trapped in the lithosphere at 45 km depth. On Venus, a high intrusive rate has been suggested to best represent the magmatic regime (Lourenço et al., 2020).

The surface melt instantaneously cools at the surface temperature, since the time span of cooling of lava flows is much faster than the time step of our models. The intrusive melt, instead, cools by conduction and leads to a local warmer lithosphere. As this locally decreases the viscosity, magmatic intrusions can lead to local lithospheric foundering and surface delamination, in particular during the early stages of evolution, even in the absence of a pseudo-plastic rheology.

The 3D grids of temperature anomalies $\Delta T(r,\theta,\phi)$ and thermal expansivity $\alpha(r,\theta,\phi)$ are then used to estimate the associated density anomalies via the relation $\Delta\rho(r,\theta,\phi) = \Delta T(r,\theta,\phi)\alpha(r,\theta,\phi)\rho_0(r)$, where $\rho_0(r)$ is the reference density profile estimated with Perple_X (Connolly, 2009) for an Earth-like mantle composition. The estimated

Table B2
Three Model Scenarios Were Investigated, Focusing on the Impact of Surface Mobilization and Lithospheric Recycling on the Polar Motion

Name	Plastic yielding	Surface mobility
MREF	No	Negligible
MMY	3×10^7 Pa	Moderate
MLY	1.88×10^7 Pa	High

density anomalies and output viscosities from the model are then used to estimate the gravitational potential at the surface using the propagator matrix technique (Richards & Hager, 1984). In this approach, gravity is computed by combining contributions from density anomalies caused by temperature variations in the mantle, as well as from flow-induced boundary deformations, both at the core-mantle boundary and at the surface (i.e., dynamic topography). The main simplification of this method is the assumption of a spherically symmetric viscosity structure, which neglects lateral viscosity variations. However, such variations are thought to be minor on Venus (Maia et al., 2023). Finally, the inertia tensor is calculated from the gravity spherical harmonic coefficients using the MacCullagh formula (Equation 6 in Rouby et al., 2010). Although the simulations are performed over 4.5 Gyrs, the moment of inertia tensors are only calculated for the past 1 Gyr of Venus' evolution since our investigation focuses on understanding the observed offset between MIA and ω at present day. Within this time period the inertia tensor is computed for all time steps output from the model, which are typically 3 Myr apart. For selected models we also performed finer sampling with a maximum of 0.3 Myr time steps. The complete list of performed models is summarized in Table B2.

Conflict of Interest

The authors declare no conflicts of interest relevant to this study.

Data Availability Statement

LIOUSHELL is an open source code, the version and input files used in this work can be downloaded from Zenodo at Patočka (2025). The folder contains inertia tensor components series that were obtained from the geoid in mantle convection simulations using code GAIA, and the 1D radial profiles of each model.

References

Austin, T. J., O'Rourke, J. G., Izenberg, N., & Silber, E. A. (2025). Survey and modeling of windblown ejecta deposits on Venus. *AGU Advances*, *6*(5), e2025AV001906. https://doi.org/10.1029/2025AV001906

Breuer, D. (2009). *4.2.3.4 dynamics and thermal evolution*. Springer Berlin Heidelberg. Berlin, Heidelberg.

Burša, M. (1984). Secular love numbers and hydrostatic equilibrium of planets. *Earth, Moon, and Planets*, *31*(2), 135–140. https://doi.org/10.1007/BF00055525

Cambiotti, G., Ricard, Y., & Sabadini, R. (2011). New insights into mantle convection true polar wander and rotational bulge readjustment. *Earth and Planetary Science Letters*, *310*(3–4), 538–543. https://doi.org/10.1016/j.epsl.2011.08.009

Cascioli, G., Durante, D., Mazarico, E., Wallace, M., Hensley, S., & Smrekar, S. (2023). Improving the VERITAS orbit reconstruction using radar tie points. *Journal of Spacecraft and Rockets*, *60*(1), 366–373. https://doi.org/10.2514/1.A35499

Cascioli, G., Hensley, S., De Marchi, F., Breuer, D., Durante, D., Racioppa, P., et al. (2021). The determination of the rotational state and interior structure of Venus with VERITAS. *The Planetary Science Journal*, *2*(6), 220. https://doi.org/10.3847/PSJ/ac26c0

Christensen, U. R. (1984). Convection with pressure- and temperature-dependent non-Newtonian rheology. *Geophysical Journal International*, *77*(2), 343–384. https://doi.org/10.1111/j.1365-246X.1984.tb01939.x

Connolly, J. A. (2009). The geodynamic equation of state: What and how. *Geochemistry, Geophysics, Geosystems*, *10*. https://doi.org/10.1029/2009GC002540

Correia, A., & Laskar, J. (2001). The four final rotation states of Venus. *Nature*, *411*(6839), 767–770. https://doi.org/10.1038/35081000

Correia, A., & Laskar, J. (2003). Different tidal torques on a planet with a dense atmosphere and consequences to the spin dynamics. *Journal of Geophysical Research*, *108*(E11). https://doi.org/10.1029/2003JE002059

Davies, M. E., Colvin, T. R., Rogers, P. G., Chodas, P. W., Sjogren, W. L., Akim, E. L., et al. (1992). The rotation period, direction of the north pole, and geodetic control network of Venus. *Journal of Geophysical Research*, *97*(E8), 13141–13151. https://doi.org/10.1029/92JE01166

Dobrovolskis, A. R., & Ingersoll, A. P. (1980). Atmospheric tides and the rotation of Venus I. Tidal theory and the balance of torques. *Icarus*, *41*(1), 1–17. https://doi.org/10.1016/0019-1035(80)90156-6

Dziewonski, A. M., Lekic, V., & Romanowicz, B. A. (2010). Mantle anchor structure: An argument for bottom up tectonics. *Earth and Planetary Science Letters*, *299*(1–2), 69–79. https://doi.org/10.1016/j.epsl.2010.08.013

Giuliani, F., Durante, D., Cascioli, G., De Marchi, F., Iess, L., Mazarico, E., & Smrekar, S. (2025). Mapping Venus's gravity field with the VERITAS mission. *The Planetary Science Journal*, *6*(1), 11. https://doi.org/10.3847/PSJ/ad991a

Grete Straume-Lindner, A., Titov, D., Ocampo Uria, A. C., & Voirin, T. (2022). The EnVision Mission to Venus (Vol. *44*).

Gross, R. S. (2000). The excitation of the Chandler wobble. *Geophysical Research Letters*, *27*(15), 2329–2332. https://doi.org/10.1029/2000GL011450

Herrick, R., & Hensley, S. (2023). Surface changes observed on a Venusian volcano during the Magellan mission. *Science*, *379*(6638), 1205–1208. https://doi.org/10.1126/science.abm7735

Hirth, G., & Kohlstedt, D. (2003). *Rheology of the upper mantle and the mantle wedge: A view from the experimentalists*. American Geophysical Union. Washington, D. C.

Hu, H., van der Wal, W., & Vermeersen, L. L. A. (2017). A full-Maxwell approach for large-angle polar wander of viscoelastic bodies. *Journal of Geophysical Research: Planets*, *122*(12), 2745–2764. https://doi.org/10.1002/2017JE005365

Hüttig, C., Tosi, N., & Moore, W. B. (2013). An improved formulation of the incompressible Navier-Stokes equations with variable viscosity. *Physics of the Earth and Planetary Interiors*, *40*, 113–129. https://doi.org/10.1016/j.pepi.2013.04.002

James, P. B., Zuber, M. T., & Phillips, R. J. (2013). Crustal thickness and support of topography on Venus. *Journal of Geophysical Research: Planets*, *118*(4), 859–875. https://doi.org/10.1029/2012je004237

Johnson, C. L., & Richards, M. A. (2003). A conceptual model for the relationship between coronae and large-scale mantle dynamics on Venus. *Journal of Geophysical Research*, *108*(E6). https://doi.org/10.1029/2002JE001962

Kohlstedt, D., Evans, B., & Mackwell, S. (1995). Strength of the lithosphere: Constraints imposed by laboratory experiments. *Journal of Geophysical Research*, *100*(B9), 17587–17602. https://doi.org/10.1029/95jb01460

Konopliv, A., Banerdt, W., & Sjogren, W. (1999). Venus gravity: 180th degree and order model. *Icarus*, *139*(1), 3–18. https://doi.org/10.1006/icar.1999.6086

Lourenço, D. L., Rozel, A. B., Ballmer, M. D., & Tackley, P. J. (2020). Plutonic-squishy lid: A new global tectonic regime generated by intrusive magmatism on Earth-like planets. *Geochemistry, Geophysics, Geosystems*, *21*(4), e2019GC008756. https://doi.org/10.1029/2019GC008756

Maia, J. S., Wieczorek, M. A., & Plesa, A.-C. (2023). The mantle viscosity structure of Venus. *Geophysical Research Letters*, *50*(15), e2023GL103847. https://doi.org/10.1029/2023GL103847

Margot, J.-L., Campbell, D. B., Giorgini, J. D., Jao, J. S., Snedeker, L. G., Ghigo, F. D., & Bonsall, A. (2021). Spin state and moment of inertia of Venus. *Nature Astronomy*, *5*(7), 676–683. https://doi.org/10.1038/s41550-021-01339-7

Matsuyama, I., Nimmo, F., & Mitrovica, J. X. (2014). Planetary reorientation. *Annual Review of Earth and Planetary Sciences*, *42*(1), 605–634. https://doi.org/10.1146/annurev-earth-060313-054724

Munk, W. H., & MacDonald, G. J. (1975). *The rotation of the Earth: A geophysical discussion*. Cambridge University Press. Cambridge, England.

Musseau, Y., Tobie, G., Dumoulin, C., Gillmann, C., Revol, A., & Bolmont, E. (2024). The viscosity of Venus' mantle inferred from its rotational state. *Icarus*, *422*, 116245. https://doi.org/10.1016/j.icarus.2024.116245

Navarro, T., & Schubert, G. (2024). Mountain waves in the upper atmosphere of Venus. *Geophysical Research Letters*, *51*(4), e2023GL104922. (e2023GL104922 2023GL104922). https://doi.org/10.1029/2023GL104922

Navarro, T., Schubert, G., & Lebonnois, S. (2018). Atmospheric mountain wave generation on Venus and its influence on the solid planet's rotation rate. *National Geographic*, *11*(7), 487–491. https://doi.org/10.1038/s41561-018-0157-x

O'Rourke, J. G., Wolf, A. S., & Ehlmann, B. L. (2014). Venus: Interpreting the spatial distribution of volcanically modified craters. *Geophysical Research Letters*, *41*(23), 8252–8260. https://doi.org/10.1002/2014gl062121

Padovan, S., Tosi, N., Plesa, A.-C., & Ruedas, T. (2017). Impact-induced changes in source depth and volume of magmatism on Mercury and their observational signatures. *Nature Communications*, *8*(1), 1–10. https://doi.org/10.1038/s41467-017-01692-0

Patočka, V. (2021). True polar wander on dynamic planets: Approximative methods versus full solution. *Journal of Geophysical Research: Planets*, *126*(12), e2021JE006948. https://doi.org/10.1029/2021JE006948

Patočka, V. (2025). Input files for: Polar motion dynamics on the slow-rotating Venus: Signatures of mantle flow [Collection]. https://doi.org/10.5281/zenodo.15862197

Patočka, V., Čadek, O., & Martinec, Z. (2018). Energy balance of glacial isostatic adjustment: Importance of the rotational feedback. *Geophysical Journal International*, *212*(2), 955–975. https://doi.org/10.1093/gji/ggx469

Patočka, V., & Kihoulou, M. (2023). Dynamic reorientation of tidally locked bodies: Application to Pluto. *Earth and Planetary Science Letters*, *617*, 118270. https://doi.org/10.1016/j.epsl.2023.118270

Patočka, V., & Walterová, M. (2025). Formula for the Chandler period (free wobble of planetary bodies). *Geophysical Research Letters*, *52*(8), e2024GL112997. https://doi.org/10.1029/2024GL112997

Pauer, M., Fleming, K., & Čadek, O. (2006). Modeling the dynamic component of the geoid and topography of Venus. *Journal of Geophysical Research*, *111*(E11). https://doi.org/10.1029/2005je002511

Phan, P.-L., & Rambaux, N. (2025). Polar motion of Venus. *Astronomy and Astrophysics*, *699*, A65. https://doi.org/10.1051/0004-6361/202553658

Revol, A., Bolmont, E., Tobie, G., Dumoulin, C., Musseau, Y., Mathis, S., et al. (2023). Spin evolution of Venus-like planets subjected to gravitational and thermal tides. *Astronomy & Astrophysics*, *674*, A227. https://doi.org/10.1051/0004-6361/202245790

Ricard, Y., Spada, G., & Sabadini, R. (1993). Polar wandering of a dynamic Earth. *Geophysical Journal International*, *113*(2), 284–298. https://doi.org/10.1111/j.1365-246X.1993.tb00888.x

Richards, M. A., & Hager, B. H. (1984). Geoid anomalies in a dynamic Earth. *Journal of Geophysical Research: Solid Earth*, *89*(B7), 5987–6002. https://doi.org/10.1029/jb089ib07p05987

Richards, M. A., Ricard, Y., Lithgow-Bertelloni, C., Spada, G., & Sabadini, R. (1997). An explanation for Earth's long-term rotational stability. *Science*, *275*(5298), 372–375. https://doi.org/10.1126/science.275.5298.372

Roberts, J. H., & Zhong, S. (2006). Degree-1 convection in the Martian mantle and the origin of the hemispheric dichotomy. *Journal of Geophysical Research*, *111*(E6), 1–18. https://doi.org/10.1029/2005JE002668

Rolf, T., Steinberger, B., Sruthi, U., & Werner, S. (2018). Inferences on the mantle viscosity structure and the post-overturn evolutionary state of Venus. *Icarus*, *313*, 107–123. https://doi.org/10.1016/j.icarus.2018.05.014

Rolf, T., Weller, A., Mattand, G., Byrne, P., O'Rourke, J. G., Herrick, R., et al. (2022). Dynamics and evolution of Venus' mantle through time. *Space Science Reviews*, *218*(8), 70. https://doi.org/10.1007/s11214-022-00937-9

Rouby, H., Greff-Lefftz, M., & Besse, J. (2010). Mantle dynamics, geoid, inertia and TPW since 120 Myr. *Earth and Planetary Science Letters*, *292*(3), 301–311. https://doi.org/10.1016/j.epsl.2010.01.033

Smrekar, S., Hensley, S., Nybakken, R., Wallace, M. S., Perkovic-Martin, D., You, T.-H., et al. (2022). VERITAS (Venus emissivity, radio science, InSAR, topography, and spectroscopy): A discovery mission.

Smrekar, S. E., Stofan, E. R., Mueller, N., Treiman, A., Elkins-Tanton, L., Helbert, J., et al. (2010). Recent hotspot volcanism on Venus from VIRTIS emissivity data. *Science*, *328*(5978), 605–608. https://doi.org/10.1126/science.1186785

Spada, G., Sabadini, R., & Boschi, E. (1996). Long-term rotation and mantle dynamics of the Earth, Mars, and Venus. *Journal of Geophysical Research*, *101*(E1), 2253–2266. https://doi.org/10.1029/95JE03222

Steinberger, B., & Torsvik, T. H. (2008). Absolute plate motions and true polar wander in the absence of hotspot tracks. *Nature*, *452*(7187), 620–623. https://doi.org/10.1038/nature06824

Stevenson, D. J., Spohn, T., & Schubert, G. (1983). Magnetism and thermal evolution of the terrestrial planets. *Icarus*, *54*(3), 466–489. https://doi.org/10.1016/0019-1035(83)90241-5

Stixrude, L., de Koker, N., Sun, N., Mookherjee, M., & Karki, B. B. (2009). Thermodynamics of silicate liquids in the deep Earth. *Earth and Planetary Science Letters*, *278*(3–4), 226–232. https://doi.org/10.1016/j.epsl.2008.12.006

Sulcanese, D., Mitri, G., & Mastrogiuseppe, M. (2024). Evidence of ongoing volcanic activity on Venus revealed by Magellan radar. *Nature Astronomy*, *8*(8), 973–982. https://doi.org/10.1038/s41550-024-02272-1

Tackley, P. J., Ammann, M., Brodholt, J. P., Dobson, D. P., & Valencia, D. (2013). Mantle dynamics in super-Earths: Post-perovskite rheology and self-regulation of viscosity. *Icarus*, *225*(1), 50–61. https://doi.org/10.1016/j.icarus.2013.03.013

Torsvik, T. H., Burke, K., Steinberger, B., Webb, S. J., & Ashwal, L. D. (2010). Diamonds sampled by plumes from the core-mantle boundary. *Nature*, *466*(7304), 352–355. https://doi.org/10.1038/nature09216

Tosi, N., Yuen, D. A., de Koker, N., & Wentzcovitch, R. M. (2013). Mantle dynamics with pressure- and temperature-dependent thermal expansivity and conductivity. *Physics of the Earth and Planetary Interiors*, *217*, 48–58. https://doi.org/10.1016/j.pepi.2013.02.004

Van Zelst, I., Crameri, F., Pusok, A. E., Glerum, A., Dannberg, J., & Thieulot, C. (2022). 101 geodynamic modelling: How to design, interpret, and communicate numerical studies of the solid Earth. *Solid Earth*, *13*(3), 583–637. https://doi.org/10.5194/se-13-583-2022

Yoder, C. F. (1995). Venus' free obliquity. *Icarus*, *117*(2), 250–286. https://doi.org/10.1006/icar.1995.1156

Yoder, C. F., & Ward, W. R. (1979). Does Venus wobble? *The Astrophysical Journal*, *233*, L33. https://doi.org/10.1086/183071

Zharkov, V. N., Gudkova, T. V., & Nikol'skii, A. (2019). On parameters of the Earth-like model of Venus. *Solar System Research*, *53*(1), 1–4. https://doi.org/10.1134/S0038094618060084